Renewable Energy 139 (2019) 483–495

Contents lists available at ScienceDirect

Renewable Energy

journal homepage: www.elsevier.com/locate/renene

Wake measurements from a hydrokinetic river turbine

Maricarmen Guerra*, Jim Thomson

Applied Physics Laboratory, University of Washington, 1013 NE 40th St, Box 355640, Seattle, WA, United States

ARTICLE INFO

Article history:
Received 13 March 2018
Received in revised form
15 November 2018
Accepted 11 February 2019
Available online 15 February 2019

Keywords:
Hydrokinetic energy
Tidal energy
Cross-flow turbine
Turbine wake
Environmental effects
Field measurements

ABSTRACT

During the boreal summer of 2015, a full-scale hydrokinetic turbine was deployed in the Kvichak River (Alaska), delivering electricity to the village of Igiugig. Here, quantification and analysis of the hydrodynamic modifications in the river caused by the turbine are presented. Field observations are used to produce a unique three-dimensional data set of fluid velocities in the vicinity of the turbine before and after turbine deployment. Three dynamic regions are distinguished in the wake. There is an induction zone just upstream of the turbine, where velocities decrease and turbulence increases. There is a near wake just downstream of the turbine, where the reduced velocities recover slightly and the elevated turbulence decays rapidly. Finally, there is a far wake well beyond the turbine, where reduced velocities are persistent and turbulence remains elevated. The results are used in a coarse energy budget for the river, including quantifying the total energy dissipated by turbulence in the near wake. This wake dissipation is found to be almost as large as the energy extracted for electricity generation, even when the turbine is not operational.

1. Introduction

Hydrokinetic energy is a predictable energy source available in streams, rivers, and tidal channels with sufficiently fast water velocities. The extraction of hydrokinetic energy for electricity generation requires the installation of hydrokinetic turbines facing the flow field. As the development of hydrokinetic turbines reaches a commercial stage, it is essential for hydrokinetic energy extraction projects to have detailed information about the hydrodynamics of these natural systems, for both turbine design and for resource assessment. In addition to ambient conditions, it is indispensable to understand and quantify the environmental impacts caused by these underwater turbines [1–3]. Specifically, the study of the wake generated by the turbines is essential in the characterization of hydrodynamic effects. Wake analysis reveals changes to the mean flow and mixing around the turbine, as well as effects farther downstream. The wake extent and its features can have an impact in the distribution and efficiency of additional turbines [4–6], and the combined wake of turbine arrays can even affect the large-scale hydrodynamics of the environment [7,8].

The wake of a hydrokinetic turbine is generally characterized by: (i) a deficit in the mean flow due to the drag produced by the turbine structure and due to energy extraction; (ii) a modification in turbulence due to eddies shed by the structure and the turbine blades; and (iii) complex interactions between natural and turbine-induced turbulent structures [6,9–11].

The idealized wake of a hydrokinetic turbine gradually expands into a cone-shaped region to conserve momentum [12]. Turbulent mixing occurs in the boundary of the region between the wake and the undisturbed flow field, bringing energy into the wake region, which smooths the velocity deficit. After several turbine characteristic length scales (typically its diameter) downstream the turbine, the wake is supposed to nearly dissipate, and the flow almost returns to original conditions [12]. Of course, the flow can never fully recover to original conditions, because kinetic energy is being extracted from the system. In some cases, the natural system converts potential energy to kinetic energy such that a pseudo-recovery can occur, but there is still a net energy loss in the extraction and subsequent wake. The development and evolution of a turbulent wake downstream of an object depends on the flow initial conditions and in the characteristics of the wake production [13,14]. Specifically, the variables that are thought to impact the turbine's wake are the rotor thrust, ambient and device induced turbulence, proximity to boundaries (bed or free surface), and the vertical and horizontal velocity profiles [12].

Much of the research on hydrokinetic turbine wakes has been carried out numerically [15–18] and at the laboratory scale under

* Corresponding author.
E-mail addresses: mguerrap@uw.edu (M. Guerra), jthomson@apl.washington.edu (J. Thomson).

https://doi.org/10.1016/j.renene.2019.02.052

simplified and controlled conditions [5,18–22]. These studies differ mainly in the type and number of turbines, and in how detailed the turbine and the energy extraction are represented [23]. Relatively few field scale measurements of turbine wakes are available in Refs. [24–26].

At the laboratory scale, turbulent flow interactions with a three-bladed, 0.5 m diameter, horizontal-axis hydrokinetic turbine and its turbulent wake were studied by Chamorro et al. [9], who observed that the velocity deficit persists beyond 15 turbine diameters at hub height (10% velocity deficit at 15 diameters downstream), and that wake recovery is enhanced by the higher shear in the top portion of the water column. The authors also observed that the velocity deficit at hub height is related to the turbine's tip-speed ratio, because the extracted power is related to this parameter.[1] In terms of turbulence intensity, this turbine wake showed variability in vertical distribution through the water column [9]. The higher levels of turbulence intensity were observed about five turbine diameters downstream of the turbine at the top portion of the wake (where the higher mean flow shear occurred in the wake), and it is reported that the increased turbulence intensity produced at depth expands and reaches the free-surface about 15 diameters downstream of the turbine [9].

The wake structure and recovery processes differ between axial-flow turbines and cross-flow turbines. Previous investigations have shown that cross-flow turbines are more efficient in wake recovery than axial-flow turbines [21]. The near-wake of a vertical cross-flow turbine was assessed by Bachant and Wosnik [21]. The near-wake of their turbine is characterized by an asymmetric velocity deficit, high-magnitude Reynolds stresses on the wake boundaries, and asymmetric turbulent kinetic energy (enhanced in the side corresponding to blade vortex shedding, were the minimum velocity deficit was found) [21]. Bachant and Wosnik [21] also identify the processes that contribute to faster wake recovery in cross-flow turbines by examining the terms in the stream-wise Reynolds-averaged Navier-Stokes (RANS) equation and in the kinetic energy balance. The authors found that wake recovery is dominated by the advection terms rather than by turbulence transport, which makes cross-flow turbines more efficient in entraining momentum into the wake when compared to axial-flow turbines [21].

The wake of a cross-flow turbine was investigated numerically in Ref. [17] by solving the Unsteady-RANS equations around a single rotating cross-flow blade in an unconfined channel. Strong deficit in all three velocity components was observed (60%), along with distinct direction patterns in vertical and cross-stream velocities. In the stream-wise direction, the wake expands both laterally and vertically, while the mean stream-wise velocity continuously increases downstream of the turbine, reaching an 85% recovery after 12 turbine diameters. Stream-wise velocity evolution downstream of the turbine is found to be dominated by cross-stream and vertical advection together with the stream-wise pressure gradient.

Despite the large amount of research regarding turbine's wakes at the numerical and laboratory scales, there is a lack of field observations in real environments, probably due to the low number of full-scale turbines deployed around the world. However, field measurements are critical for validating numerical results and for scaling laboratory experiments results, as well as for estimating the true environmental effects of hydrokinetic energy extraction at each location.

This paper presents comprehensive field observations of the wake from a full-scale hydrokinetic turbine under natural flow conditions. Specifically, a detailed characterization of Ocean Renewable Power Company (ORPC) RivGen turbine wake in the Kvichak River (Alaska) is reported. The site and turbine details together with the measurements methodology are presented in section 2. Section 3 presents a description of the wake in terms of mean flow and turbulence parameters. A discussion on the wake evolution, on the wake of a non-operational turbine, and on the wake energy loss is presented in section 4, followed by Conclusions in section 5.

2. Methods

2.1. Site and turbine description

The Kvichak River, located in southwest Alaska, drains the Iliamna Lake flowing southwest towards Bristol Bay. The turbine deployment site is about 2 km downstream from the Iliamna Lake, next to the village of Igiugig, where the river is approximately 5 m deep and 150 m wide. The flow is at is maximum, $\sim 2.5\ \mathrm{ms^{-1}}$, in the center of the river. Fig. 1a shows a map of the Kvichak River bathymetry on top of a Google Earth image of the area, together with the location of the turbine deployment site: N 59° 19.495′; W 155° 54.890′.

The ORPC RivGen turbine is a horizontal cross-flow hydrokinetic turbine rated at 35 kW [29]. The turbine consists in two rotors plus a generator located in between the rotors. The entire turbine is 11.5 m wide. Each rotor is 1.5 m in diameter and 4.1 m wide. Turbine hub-height at this location was approximately 2.5 m below the river free surface when the turbine was submerged and resting on the riverbed. Turbine blockage in the Kvichak River was 10% when considering the turbine swept area plus the turbine's support structure area over the area of the river cross-section at the turbine location. Rotors swept area represented 3% of the total blockage, and rotor height covered approximately 25% of the water column. On the turbine's lateral ends, the pontoon support structure and turbine rotors total height is 3.3 m, which resulted in a vertical blockage of 55%. Details of turbine performance in the Kvichak River can be found in Refs. [29,30]. A picture of ORPC RivGen prior to its deployment is shown in Fig. 1b.

2.2. Data collection

Hydrodynamic data were collected in the area surrounding RivGen prior to and after its deployment in July 18th, 2015. A new version (v4β) of the SWIFT drifter buoy [31] was used to measure surface velocity and velocity fluctuations along the water column (Fig. 2). Table 1 summarizes all instrument deployments and settings.

A Nortek Signature1000 five-beam acoustic Doppler current profiler (AD2CP) was mounted down-looking on a disk buoy (SWIFT), which was equipped with two Qstarz GPS data receivers. The Signature1000 measured along-beam velocities trough the water column as it was drifting using its five beams at 8 Hz in broadband mode. There were 14 depth bins separated by 0.5 m, and a 0.5-m blanking distance. Single ping error, σ_b, reported by the instrument manufacturer is $0.05\ \mathrm{ms^{-1}}$ for the along-beam velocities. The GPS measured geographic position, drifting velocity, and heading at 10 Hz, with a 5-m accuracy in position and $0.05\text{-}\mathrm{ms^{-1}}$ in drifting velocity (using a phase-resolving GPS antenna).

Drifts began ~ 200 m upstream of the turbine location by releasing the drifter from a small vessel. The drifter was released at different positions across the river to follow different surface streamlines across the river. After each drift, the SWIFT was recovered ~ 200 m downstream of the turbine.

Two sets of drifts were conducted: before and after turbine

[1] For general turbine characteristics and performance parameters refer to Burton et al. [27] and Batten et al. [28].

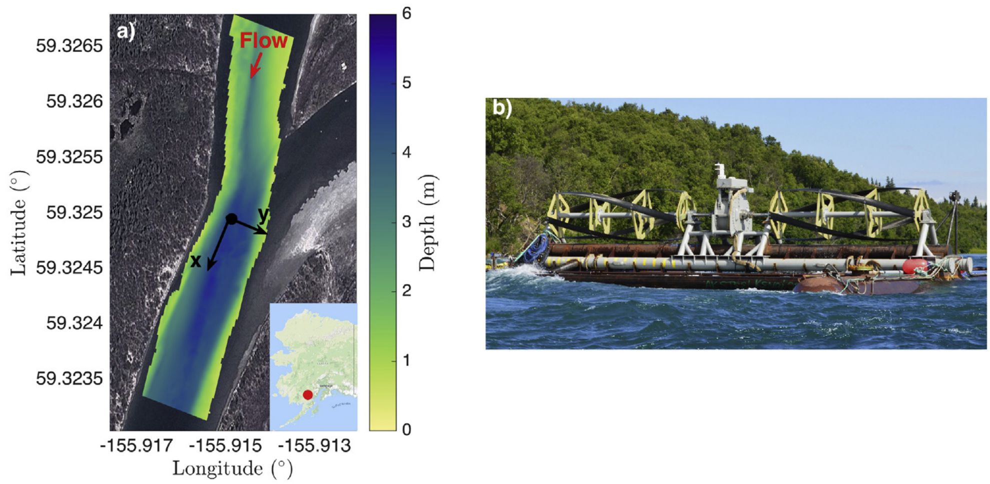

Fig. 1. a) Google Earth image of the Kvichak River and river bathymetry in colors. Black dot shows turbine location, and black arrows identify the local coordinate system used for the wake analysis. Red arrow represents the flow main direction. Red dot in the inset map shows study location within Alaska. b) Downstream view of ORPC RivGen prior to its deployment in July 2015. (For interpretation of the references to color in this figure legend, the reader is referred to the Web version of this article.)

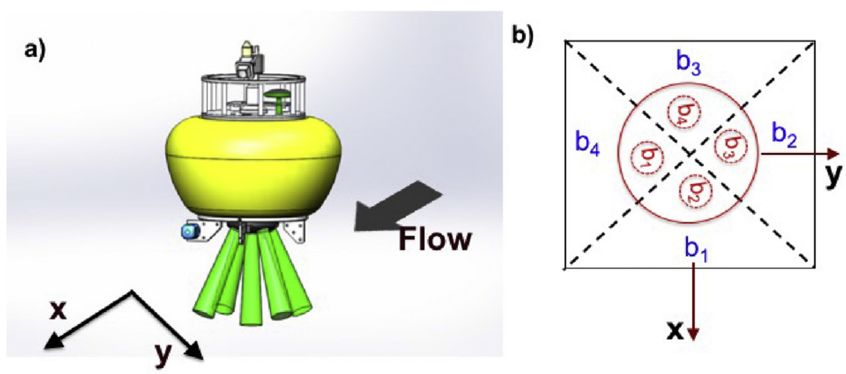

Fig. 2. a) SWIFT v4 prototype schematic (rendered by Alex de Klerk, APL-UW). Green cone-shaped areas illustrate the Nortek Signature1000 along-beam velocity directions. b) Plan-view of a single horizontal grid cell illustrating the pseudo-along-beam velocities local system. In red is an example of misaligned along-beam velocities from the Signature1000. (For interpretation of the references to color in this figure legend, the reader is referred to the Web version of this article.)

Table 1
Summary of deployments and sampling parameters at the Kvichak River.

Condition	Undisturbed river	Undisturbed river	Non-operational turbine	Operational turbine
Instrument	Nortek Vector	Nortek Signature 1000	Nortek Signature 1000	Nortek Signature 1000
Platform	Vessel with davit	SWIFT drifter	SWIFT drifter	SWIFT drifter
Dates	8–13 July 2015	8–13 July 2015	19 July 2015	20–21 July 2015
Hold Stations/Drifts	35	150	40	150
Sampling Frequency (Hz)	16	8	8	8
z target (m)	−2.5	–	–	–
Δz (m)	–	0.5	0.5	0.5
Distance to first cell (m)	–	0.25	0.25	0.25
Range (m)	–	7	7	7
Single ping error (ms^{-1})	0.02	0.05	0.05	0.05

deployment. The first set characterized the undisturbed river. This data set consisted of 150 drifts between July 8th and July 13th, 2015. A portion of the drifts (15) were set-up to measure altimetry (bathymetry) with additional pings, and this restricted along-beam velocity sampling to 4 Hz (instead of 8 Hz).

The second set of drifts was conducted after turbine deployment, from July 19th to July 21st, 2015. On July 19th, the turbine was underwater but non-operational (braked), while on July 20th and 21st, the turbine was operational and delivering electricity to the grid. There were 40 drifts while the turbine was non-operational, and 150 while it was operational. These data sets covered the same longitudinal river span as for the undisturbed conditions, but concentrated drifts over and next to the turbine to evaluate the turbine wake. As for the first set, 25 drifts were taken in altimeter mode, measuring along-beam velocities at 4 Hz.

Data from the Signature1000 were quality controlled by removing measurements with low beam correlations (less than 30) and low echo amplitude (less than 80 dB). This process allowed to remove all data recorded while the SWIFT was outside of the water, and to detect the riverbed (or any solid boundary) and remove data below it.

An additional data set was obtained prior to turbine deployment using a Nortek Vector acoustic Doppler velocimeter (ADV) in order to provide ORPC with upstream turbine flow conditions and to test the accuracy of the drifting method measurements. The ADV was mounted on a turbulence torpedo (TT), a sounding weight that hangs from a davit on the aft of a small vessel while the vessel holds station [32,33]. The ADV targeted turbine hub-height (2.5 m below the river free surface) at several locations around the turbine site. Vessel location and drifting velocity were recorded using two Qstarz GPSs located on top of the davit. The ADV sampled turbulent velocities at 16 Hz for about 20 min at each targeted location. ADV data were quality-controlled to remove data with low correlation and low echo amplitude, and despiked using the 3D phase space method of Goring and Nikora [34]. The ADV data were organized in 1-min ensembles and screened by vessel drift velocity, where data with an ensemble-averaged vessel drift velocity higher than $0.5\ \mathrm{ms}^{-1}$ were removed (not holding station). Additional motion contamination from the deployment platform was removed by applying the methods presented in Ref. [33].

To make the data sets comparable, it is essential to assume steady state conditions (in the mean flow sense) in the Kvichak River during the measurements periods. This assumption is evaluated in A.

2.3. Coordinate systems

A local coordinate system is defined (shown in Fig. 1a) to organize the data, with x oriented in the stream-wise direction, y in the cross-stream direction, and z in the vertical direction (positive upward). The local coordinate system origin is at the free surface at the nominal center of the turbine (N 59° 19.495′; W 155° 54.890′), and the local axis of rotation from an east-north-up (true) coordinate system is 107° clockwise from north. The same coordinate system is used to define river velocities, with x corresponding to the stream-wise velocity u, y corresponding to the cross-stream velocity v, and z corresponding with the vertical velocity w. The location of each measurement, originally in latitude and longitude, is mapped to the local coordinate system.

Following the coordinate transformation, all data sets (including the data from the turbulence torpedo ADV) are organized by location in a three-dimensional, structured, uniform grid defined in local coordinates. The grid is of 2 m horizontal resolution, with 0.5 m vertical resolution (coincident with the Signature1000 velocity bins). The grid extends from −200 m to 200 m in x, from −60 to 60 m in y, and from 0 to −7 m in z. The ADV data set grid contains data only at $z = -2.5$ m, corresponding to turbine hub-height.

Within each grid cell two data products are constructed: true Eulerian velocities and pseudo-along-beam velocities, which are used to define river mean flow and turbulence parameters, respectively.

2.3.1. True Eulerian velocities

Velocities captured by the drifting Signature1000 correspond to fluctuations from the surface drifting velocity. All recorded velocities (from the GPS and from the Signature1000) are converted to east-north-up (ENU) velocities, and subsequently converted to velocities in the local coordinate system (u, v, and w). True Eulerian velocity profiles in the local coordinate system are constructed as:

$$u(x,y,z,t) = u_{\mathrm{GPS}}(x,y,t) + u_{\mathrm{Sig}}(x,y,z,t), \tag{1}$$

$$v(x,y,z,t) = v_{\mathrm{GPS}}(x,y,t) + v_{\mathrm{Sig}}(x,y,z,t), \tag{2}$$

where u and v correspond to the horizontal components of velocity in the local coordinate system, the GPS subscript represents drifting velocity components recorded by the GPS, and the Sig subscript represents velocity components recorded by the Signature1000. Vertical profiles of vertical velocities w do not need to be reconstructed as they are directly recorded by the vertical beam of the Signature1000.

2.3.2. Pseudo-along-beam velocities

During these measurements, instrument horizontal rotation could not be controlled, thus the heading of the Signature1000 changed within each drift. Then, within each grid cell, the raw along-beam velocities recorded by the Signature1000 might not have coincided in direction, hence no time-series of along-beam velocities can be directly obtained. A fixed local system of four pseudo-along-beam velocities directions is defined within each grid cell to resolve this issue. In the new system, the horizontal component of each pseudo-along-beam velocity corresponds to the direction of the local coordinate system axis: the horizontal component of b_1 corresponds to the positive x-axis, the one from b_2 corresponds to the positive y-axis, the one from b_3 corresponds to the negative x-axis, and the one from b_4 corresponds to the negative y-axis direction. The pseudo-along-beam velocity coordinate system is shown in Fig. 2b together with an example of the misalignment between the local-coordinate system and the Signature1000 along-beam velocities.

For each measurement, the pseudo-along-beam velocities are constructed based on the heading recorded by the Signature1000, because the heading indicates the direction of the recorded along-beam velocities with respect to the local coordinate system. First, a heading with respect to the local x-axis is estimated as $H_x = H - 17^\circ$, where H is the instrument heading and H_x is the local heading. When $H_x = 180^\circ$, the instrument x-axis is aligned with the local x-axis. Within a grid cell, the construction of pseudo-along-beam velocities is based on four heading scenarios. Each scenario corresponds to a 90° angular cell centered in the direction of the local coordinate system axis. These scenarios and the corresponding pseudo-along-beam velocities definitions are listed in Table 2.

2.4. Mean flow parameters

Mean flow parameters are obtained from the true Eulerian velocities estimated within each grid cell. These parameters are used to characterize and quantify the hydrodynamic effects of RivGen in the Kvichak River.

At each grid cell, a non-uniform time series of true Eulerian

Table 2
Pseudo-along-beam velocities based on instrument heading with respect to local coordinate system x-axis.

Pseudo-along-beam velocity	$135^\circ < H_x < 225^\circ$	$225^\circ < H_x < 315^\circ$	$315^\circ < H_x < 45^\circ$	$45^\circ < H_x < 135^\circ$
b_1	b_{1Sig}	b_{2Sig}	b_{3Sig}	b_{4Sig}
b_2	b_{2Sig}	b_{3Sig}	b_{4Sig}	b_{1Sig}
b_3	b_{3Sig}	b_{4Sig}	b_{1Sig}	b_{2Sig}
b_4	b_{4Sig}	b_{1Sig}	b_{2Sig}	b_{3Sig}

velocity components is available. Assuming steady-state conditions in the Kvichak River during the field measurements (see A), these time-series are averaged to obtain a single velocity vector at each grid-cell. All velocity measurements are affected by the intrinsic noise of the instruments that measures them. For this case, the velocity measurements are affected by the GPS velocity uncertainty and by the inherent Doppler noise of the Signature1000. After time-averaging the velocities, the horizontal velocity component uncertainty within each grid cell, σ_u, is defined as:

$$\sigma_u = \sqrt{\frac{\sigma^2_{u_{\mathrm{Sig}}}}{N} + \frac{\sigma^2_{u_{\mathrm{GPS}}}}{N}}, \tag{3}$$

where $\sigma_{u_{\mathrm{Sig}}}$ is the horizontal velocity uncertainty from the Signature1000, $\sigma_{u_{\mathrm{GPS}}}$ is the uncertainty of the velocity recorded by the GPS on board the SWIFT buoy, and N is the number of velocity measurements available for each grid cell.

Using the time-averaged velocity vector at each grid cell, velocity shear is estimated by a centered finite difference scheme. A coarse vorticity is then estimated using the estimated discrete shear in all three Cartesian directions. The shear of the along-channel velocity component u in the x direction, and its uncertainty, are defined as:

$$\frac{\mathrm{d}u}{\mathrm{d}x} = \frac{u_{i+1,j,k} - u_{i-1,j,k}}{2\Delta x}, \tag{4}$$

$$\sigma_{Shear} = \frac{1}{2\Delta x}\sqrt{\sigma^2_{u_{i+1,j,k}} + \sigma^2_{u_{i-1,j,k}}}, \tag{5}$$

where i, j, and k represent each grid cell and u is the x-axis velocity component. The velocity shears in the other directions, and for the rest of the velocity components (v and w), follow the same definition.

Additional mean flow parameter uncertainties arise from the error in the GPS locations and from natural variability within a grid cell. These are assumed to be uncorrelated, and averaging within the grid cells significantly reduces them.

2.5. Turbulence parameters

Turbulence parameters are obtained following the methods presented in Ref. [35] for a five-beam acoustic Doppler profiler, which are based on the variance of along-beam turbulence fluctuations. For this investigation, the pseudo-along-beam velocity fluctuations are used instead.

A pseudo-turbulence intensity, (pTI), is estimated using the pseudo-along-beam velocity variances, $\overline{b'^2_i}$, relative to the mean flow velocity at each depth. The noise-corrected pTI is defined as:

$$pTI(x,y,z) = \frac{\sqrt{\frac{1}{5}\sum_{i=1}^{5}\overline{b'^2_i}(x,y,z,t) - \sigma^2_b}}{U(x,y,z)}, \tag{6}$$

where b_i represents each pseudo-along-beam velocity, σ^2_b is the along-beam velocity noise variance [36], and U is the horizontal velocity magnitude. The pseudo-along-beam measurements have independent noise errors, σ_b, and thus using of all five pseudo-along-beam velocities is preferred to estimate the velocity variations at each grid cell. By only using the pseudo-along-beam velocities, pTI only captures the turbulent length scales similar to the beam separations. This spatial definition is uniformly biased low compared to the usual temporal definition of turbulent intensity $\sigma_U/\overline{U}$, where σ_U is the standard deviation of the flow velocity and $\overline{U}$ is the mean flow velocity.

The five-beam configuration of the Signature1000 facilitates the estimation of five out of six Reynolds stresses [35]. Assuming zero-mean pitch and roll within each grid cell, the noise-corrected Reynolds stresses are defined using the variance of the pseudo-along-beam velocity fluctuations as:

$$\overline{u'^2} = \frac{\overline{b'^2_1} + \overline{b'^2_3} - 2\overline{b'^2_5}\cos^2\theta}{2\sin^2\theta} - \sigma^2_b, \tag{7}$$

$$\overline{v'^2} = \frac{\overline{b'^2_2} + \overline{b'^2_4} - 2\overline{b'^2_5}\cos^2\theta}{2\sin^2\theta} - \sigma^2_b, \tag{8}$$

$$\overline{w'^2} = \overline{b'^2_5} - \sigma^2_b, \tag{9}$$

$$\overline{u'w'} = \frac{\overline{b'^2_3} - \overline{b'^2_1}}{4\sin\theta\cos\theta}, \tag{10}$$

$$\overline{v'w'} = \frac{\overline{b'^2_4} - \overline{b'^2_2}}{4\sin\theta\cos\theta}, \tag{11}$$

where $\overline{b'^2_i}$ corresponds to the pseudo-along-beam velocity variances, and θ is the beam inclination angle (25° for the Signature1000), and σ^2_b corresponds to the noise variance from the Signature1000. $\overline{u'^2}$ corresponds to the along-channel turbulent kinetic energy (TKE), which can be used to estimate an along-channel turbulence intensity, TI, as:

$$TI(x,y,z) = \frac{\sqrt{\overline{u'^2}}}{U(x,y,z)}. \tag{12}$$

Both the along-channel turbulence intensity and the along-channel TKE are used to measure how the turbulence evolves downstream of the turbine.

The TKE dissipation rate, ε, is estimated through the second-order spatial function of the along-beam velocity fluctuations $D(z,r)$ [35,37]. This methodology requires the observation of the inertial sub-range of isotropic turbulence. Using the vertical beam velocity fluctuations, within each grid cell, the structure function is defined as:

$$D(z,r) = \overline{\left[b'_5(z+r) - b'_5(z)\right]^2}, \tag{13}$$

where z is the along-beam measurement location, b'_5 corresponds to the velocity fluctuation along the vertical beam, and r is the distance between two velocity bins; the overline denotes time-average. In the inertial subrange of isotropic turbulence, the structure function is related to the distance r by:

$$D_i(z,r) = C^2_v \varepsilon^{2/3} r^{2/3}, \tag{14}$$

where $C^2_v = 2.1$ is a constant [36,37].

The structure function is estimated using all instantaneous profiles within each grid cell, which correspond to a non-uniform time series. Then, the structure function is multiplied by $r^{-2/3}$ to obtain a compensated structure function in the inertial subrange [38]. The TKE dissipation rate, ε, is estimated by solving $\overline{D(z,r)r^{-2/3}|^{r_2}_{r_1}} = C^2_v\varepsilon^{2/3}$, where r_1 to r_2 is the range where the compensated structure function slope is closest to zero, and the overline denotes the average. Estimates are not calculated for depths with less than four points in the structure function, hence r values ranged between 2 m and 7 m.

Uncertainties in ε from the structure function fitting are calculated by propagating the uncertainty in the compensated structure function such that:

$$\sigma_{\varepsilon_D} = \left(\frac{1}{Cv^2}\right)^{3/2} \frac{3}{2} \overline{D_{comp}}^{1/2} \sigma_{D_{comp}}, \tag{15}$$

where $\sigma_{D_{comp}}$ corresponds to the standard deviation of the compensated structure function in the r range used for the computations.

2.6. Data-products comparison

Flow parameters obtained from the SWIFT data set are compared with those obtained from the ADV data set for the undisturbed river conditions to test the accuracy of the drifting method. Data are compared in terms of the velocity magnitude, pseudo turbulence intensity, turbulence intensity, and TKE dissipation rate. ADV-based flow parameters are obtained similarly to those from the SWIFT buoy, with the exception of TKE dissipation rate, which is estimated through the TKE spectra derived from the ADV measurements [35]. Fig. 3 compares grid cell flow parameters (in blue), and grid longitudinal averages (in gray) as longitudinal homogeneity was observed in the area covered by the ADV measurements.

Overall there is a good agreement between flow parameters obtained from SWIFT data set and those from the ADV data set. Excellent agreement is observed for the gridded velocity magnitude between both measurement methods, with an $RSME = 0.16$ ms^{-1} between the values from the SWIFT and the values from the TT-ADV platform. Good linear agreement is found between the pseudo-turbulence intensity from both data sets, with an $RSME = 4\%$. However, the pseudo-turbulence intensity from the SWIFT data set is biased low (the linear fit slope is 0.6). This bias is expected, because the *pTI* only considers a portion of the turbulence length-scales, while the turbulence intensity from TT-ADV is estimated through its usual definition and considers all turbulence length-scales in the along-channel direction. Fig. 3c shows turbulence intensity estimated using equation (12). Although significant scatter in the plot is observed, a linear trend and good agreement is found between the longitudinal averages, with an $RSME = 2\%$ and a best linear fit slope of 1.29.

The TKE dissipation rate estimates from the TT-ADV tends to be larger than those from the SWIFT. Despite the scatter in the comparison of these turbulence parameters, the average values obtained from the two methods are of the same order of magnitude. This is notable, given the large dynamic range of this quantity in the natural environment.

Differences are attributed to uncertainties in the location of the measurements (from the GPS receivers), by remaining noise in the parameter estimates, and by differences in the methods. Specifically, the ADV measurements provide data-dense time series of flow parameters within each grid cell, while the SWIFT measurements provides spatial averages from non-uniformly sampled sparse data.

3. Results: wake characterization

The RivGen wake in the Kvichak River is characterized by the previously defined flow parameters obtained from the repeated

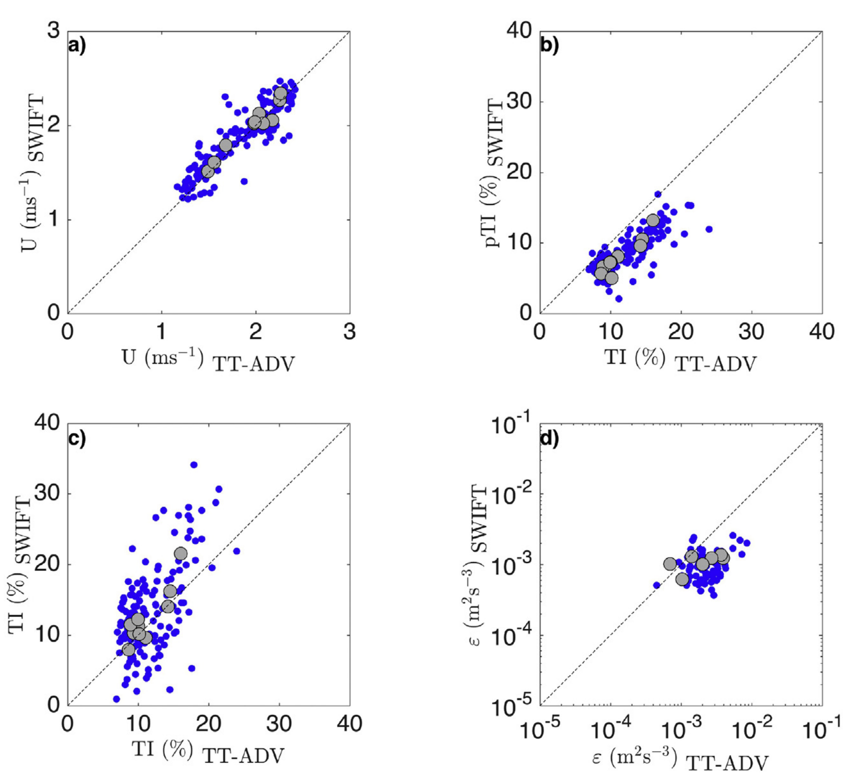

Fig. 3. Comparison of flow parameters between ADV data (x-axis) and SWIFT data (y-axis) for the undisturbed river condition: a) Velocity magnitude U, b) pseudo-turbulence intensity *pTI*, c) turbulence intensity *TI*, and d) TKE dissipation rate ε. Blue dots correspond to grid cell parameters, and larger gray dots correspond to longitudinal averages of grid cell values. Dotted lines correspond to the $y = x$ in all plots. (For interpretation of the references to color in this figure legend, the reader is referred to the Web version of this article.)

SWIFT drifts. In general, the wake signal is strong and noticeable in all estimated flow parameters. In what follows, the undisturbed river conditions and post-turbine deployment flow conditions are presented, always considering an operational RivGen. (The braked, non-operational RivGen will be considered in the Discussion.) Plan and longitudinal views of the river are presented, colored by the different mean flow and turbulence parameters. All plan views correspond to hub-height ($z = -2.5$m), while longitudinal views correspond to a streamline passing through the center of the turbine shown as a gray dotted line in Fig. 4b. The turbine location ($x = 0, y = 0$) is represented by a black rectangle in all plan views. In the longitudinal views, the turbine is represented by a gray oval due to the different scales of the horizontal and vertical axis. In these plots the black rectangle corresponds to data removed due to turbine and support structure interference with the ADCP pings.

3.1. Mean flow parameters

Fig. 4a shows contours of grid-averaged velocity magnitude at hub-height for undisturbed river conditions. The undisturbed flow is stronger mid-river, reaching about 2.3 ms^{-1} at the turbine location ($(x, y) = (0, 0)$), while slower flows are observed towards the river banks. When the river is undisturbed, strong lateral shear is observed at the cross-section corresponding to the turbine location, with stronger flows towards the Igiugig side of the river (positive y-axis).

A plan view of velocity magnitude at hub-height while the turbine is operational is presented in Fig. 4b. The turbine wake is observed immediately downstream of the turbine. Velocity magnitude is dramatically reduced, from 2.3 ms^{-1} to 1 ms^{-1} at the turbine location and slower velocities are observed beyond 200 m downstream of the turbine. The wake remains mostly laterally constrained by the prevailing shape and direction of the river. Closer to the free-surface (above hub-height), the wake from the two turbine rotors can be distinguished, together with a reduced wake from the generator (located between the two rotors). These features are mixed about 40 m downstream of the turbine.

Fig. 5 shows a longitudinal profile of the river colored by velocity magnitude. In its undisturbed state, classical open channel flow is observed in the river. The turbine wake has a rich longitudinal structure. The velocity decrease begins upstream of the turbine, as the river flow encounters the turbine and slows down. Flow accelerates on top of the turbine, indicating vertical blockage effects.

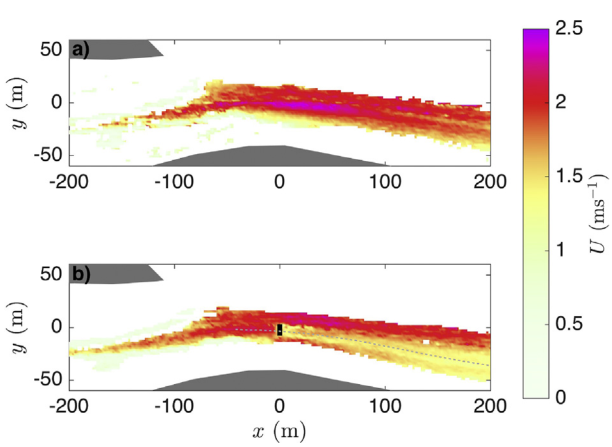

Fig. 4. Plan view of horizontal velocity magnitude U at hub-height (2.5 m below the river free surface). a) undisturbed river, and b) when turbine is underwater and operational. Flow is from left to right. Gray dashed line in a) shows location of center streamline used for the longitudinal plots. Black rectangle shows turbine location.

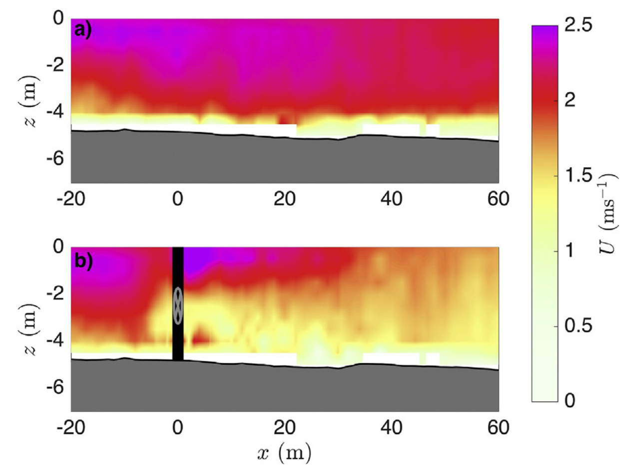

Fig. 5. Longitudinal view of horizontal velocity magnitude U along a center streamline (shown in Fig. 3a). a) undisturbed river, and b) when turbine is underwater and operational. Flow is from left to right.

During the field measurements, a small free-surface decrease was observed visually at the turbine location, but it was not captured by the GPS vertical elevation measurements on the drifter (presumably because of insufficient vertical accuracy).

Downstream of the turbine the wake expands vertically reaching the free-surface about 35 m away from the turbine, as observed in the surface velocities recorded by the GPS on board the SWIFT buoy.

Average uncertainty in the velocity estimates prior to turbine deployment is 1.3 cms^{-1}, and 1.2 cms^{-1} when the turbine is operational.

In its undisturbed state, the Kvichak River has a vertical vorticity (ω_z) in opposite direction along the Igiugig side of the river (positive y-axis), probably due to a lateral sharp change in bathymetry (Fig. 6a). The presence of the turbine has a strong impact on vertical vorticity, generating sufficient vertical vorticity to reverse the sign at the lateral edges of the turbine, showing the expected behavior for an obstacle in the flow (Fig. 6b. Cross-stream vorticity, ω_y, is shown in Fig. 7). Baseline cross-stream vorticity is maximum near

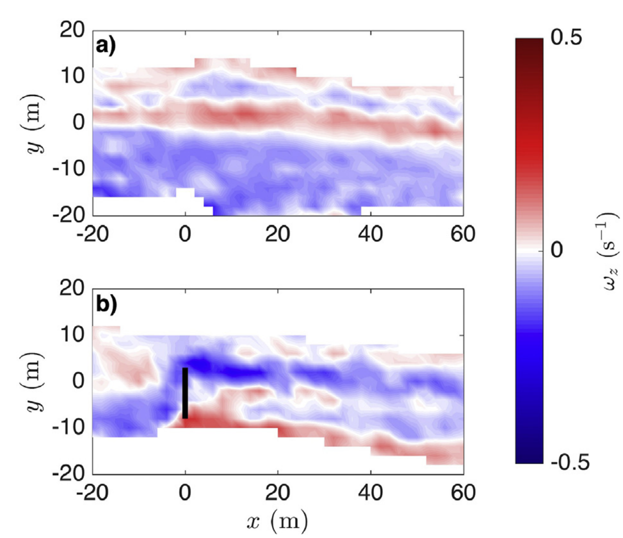

Fig. 6. Plan view of vertical vorticity ω_z at hub-height (2.5 m below river free surface). a) undisturbed river, and b) when turbine is underwater and operational. Flow is from left to right.

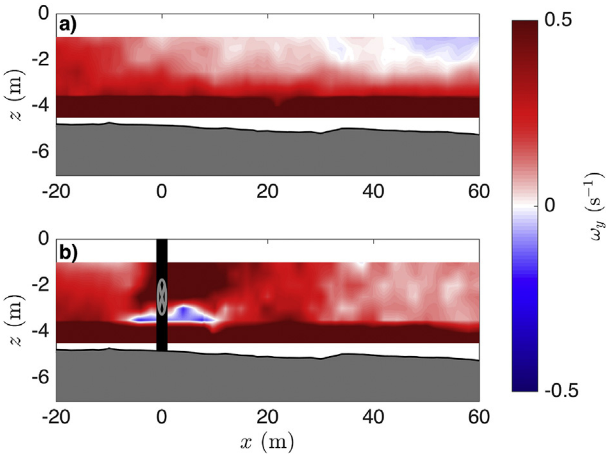

Fig. 7. Longitudinal view of cross-channel vorticity ω_y along a center streamline (shown in Fig. 3a). a) undisturbed river, and b) when turbine is underwater and operational. Flow is from left to right.

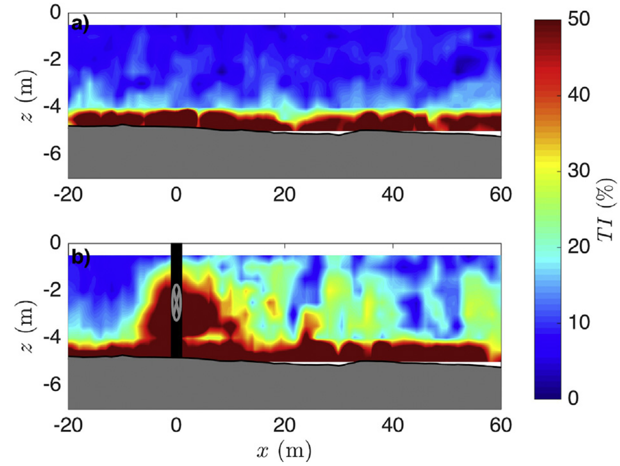

Fig. 9. Longitudinal view of turbulence intensity *TI* along a center streamline (shown in Fig. 3a). a) undisturbed river, and b) when turbine is underwater and operational. Flow is from left to right.

the bottom, consistent with bottom-induced vorticity. Similarly, when the turbine is underwater, cross-stream vorticity is enhanced above and below the turbine, and vorticity direction is coincident with increased vorticity observed for flow passing around a cylinder. However, the wake vorticity magnitude is asymmetric, similar to what was observed in laboratory experiments, even under different conditions boundary [21]. This asymmetry is explained by blade rotation, which induces cross-stream vorticity in the opposite direction. For the non-operational condition, cross-stream vorticity below the turbine, is similar to cross-stream vorticity observed above the turbine. Average uncertainty is 0.04 s^{-1} for the vertical vorticity and 0.1 s^{-1} for the cross-stream vorticity.

3.2. Turbulence parameters

Figs. 8 and 9 show maps of turbulence intensity estimated as the ratio between the standard deviation of the along-channel turbulence fluctuations and the along-channel velocity. Natural river turbulence intensity is about 10% through the water column. Larger values of turbulence intensity are observed near the bottom and in the shallower areas of the river, consistent with bottom-generated turbulence and slower flows. When the turbine is deployed, a region of elevated turbulence intensity is observed in the area surrounding it. Turbulence intensity increases more than five times from its original level due to both an increase in velocity fluctuations (up to five times) and a decrease in mean velocity. Unlike the mean velocity, the turbulence intensity, and the TKE, decrease rapidly downstream of the turbine, reaching a level similar to the natural river conditions. As shown in the plan-view plot of Fig. 8b, the turbulence intensity of the wake decreases in width, concentrating the elevated turbulence intensity mid-river.

The turbine effects are also observed in the Reynolds stresses, which represent turbulent momentum transport in the wake. Although estimates are noisy, elevated Reynolds stresses are observed up to 20 m downstream of the turbine, suggesting that turbulent transport is important in this region. Figs. 10 and 11 show contour maps of the $\overline{u'w'}$ Reynolds stress. The regions of strong $\overline{u'w'}$ correspond to regions of velocity shear, which are caused by the decrease in velocity; the net effect is consistent with increased TKE production.

TKE dissipation rate maps are shown in Figs. 12 and 13. Downstream of the turbine, TKE dissipation rate increases by at least a

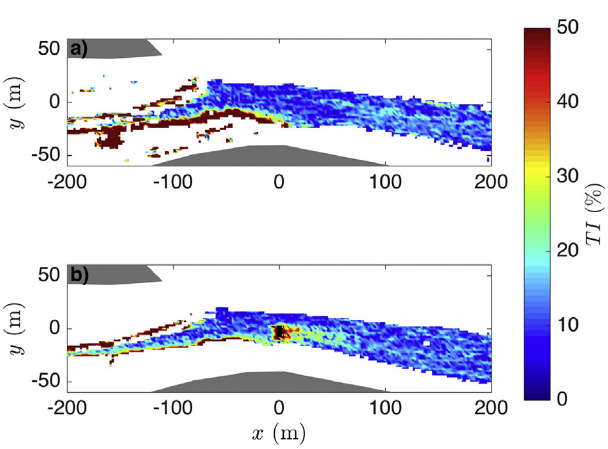

Fig. 8. Plan view of total turbulence intensity *TI* at hub-height (2.5 m below river free surface). a) undisturbed river, and b) when turbine is underwater and operational. Flow is from left to right.

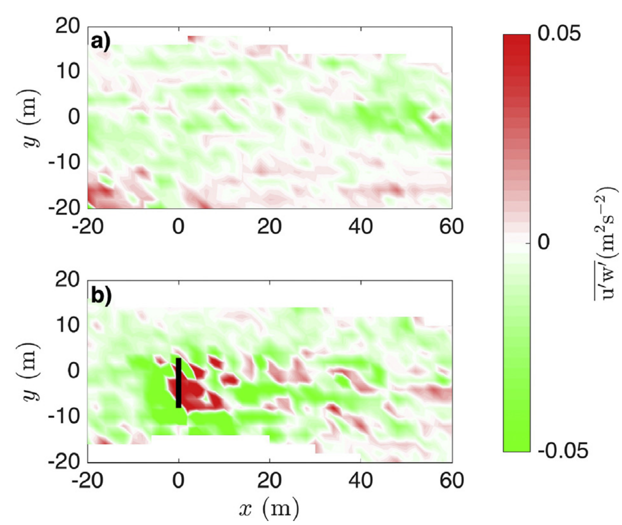

Fig. 10. Plan view of $\overline{u'w'}$ Reynolds stress at hub-height (2.5 m below river free surface). a) undisturbed river, and b) when turbine is underwater and operational. Flow is from left to right.

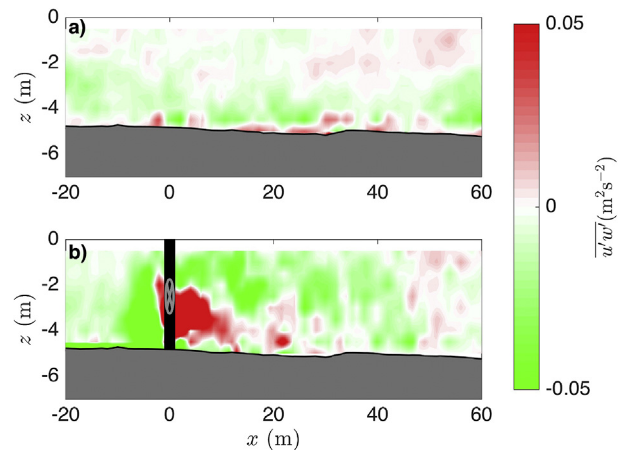

Fig. 11. Longitudinal view of $\overline{u'w'}$ Reynolds stress along a center streamline (shown in Fig. 3a). a) undisturbed river, and b) when turbine is underwater and operational. Flow is from left to right.

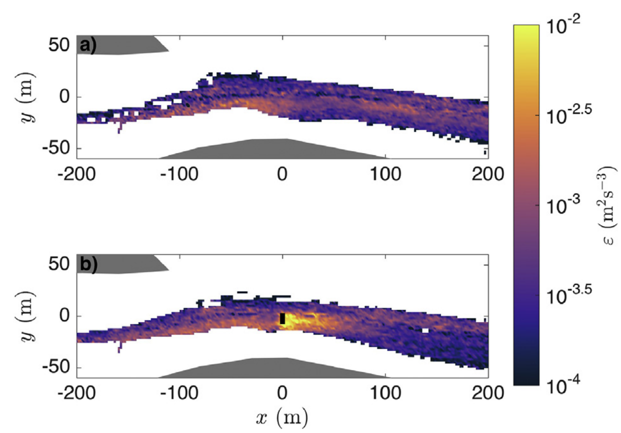

Fig. 12. Plan view of TKE dissipation rate ε at hub-height (2.5 m below river free surface). a) undisturbed river, and b) when turbine is underwater and operational. Flow is from left to right.

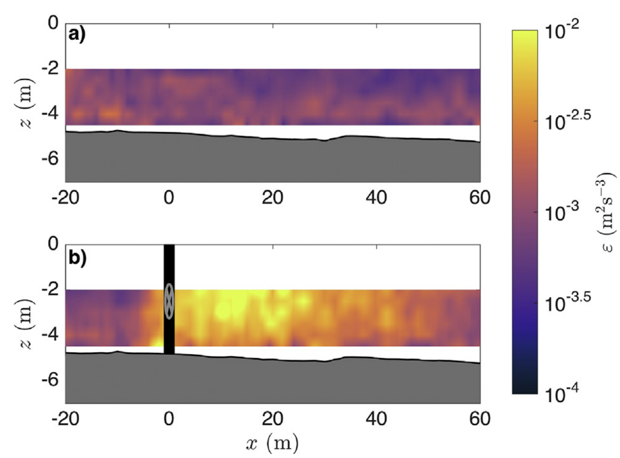

Fig. 13. Longitudinal view of TKE dissipation rate ε along a center streamline (shown in Fig. 3a). a) undisturbed river, and b) when turbine is underwater and operational. Flow is from left to right.

decade, consistent with the increase in turbulent kinetic energy. Along the center streamline, TKE dissipation rates are elevated throughout the entire water column. Although TKE dissipation rates decrease downstream of the turbine, they remain above baseline values for about 60 m downstream of the turbine. Average uncertainty in the TKE dissipation rate estimates is 4.4 $\times 10^{-4}$ m^{2}s^{-3} prior to turbine deployment, and it is 7.6 $\times 10^{-4}$ m^{2}s^{-3} when the turbine is operational.

4. Discussion

4.1. Wake evolution

Fig. 14 compares horizontal and vertical profiles of velocity at different distances from the turbine for the undisturbed river and when the turbine is operational. Horizontal profiles taken at hub-height show a strong wake signal from the two rotors and the generator. The profiles slowly mix horizontally, however the wake signal is still clearly observed 50 m downstream of the turbine. Vertical profiles, taken along the center streamline shown in Fig. 4b, show the sharp decrease in velocity at hub-height. Closer to the turbine, at $x = 2$ m, the velocity vertical profile shows the accelerated flow on top of the turbine. The velocity mixes vertically about 50 m downstream of the turbine, and typical logarithmic open channel profiles are observed. However, velocities remain slower compared to the undisturbed vertical profiles due to energy extraction. These differences suggest that in this shallow river the velocity profiles homogenize faster vertically than horizontally, probably as a result of bottom-induced shear stress.

In what follows, the along-channel TKE ($\overline{u'^2}$) is used to study the wake evolution instead of the turbulence intensity, because it provides information about the turbulence evolution rather than a ratio to the mean flow.

Longitudinal profiles of hub-height velocity (U), along-channel TKE ($\overline{u'^2}$), and TKE dissipation rate (ε), are presented in Fig. 15. In these plots, the lines in dark colors represent the average across three streamlines: along the turbine port side, along the turbine center (shown in Fig. 4), and along the turbine starboard side. Shadows represent the standard deviations across the three

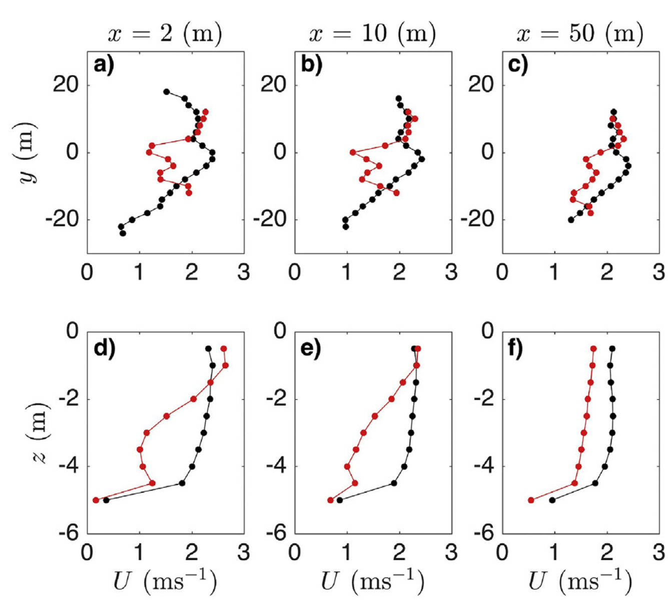

Fig. 14. Horizontal and vertical profiles of velocity magnitude U at three different locations downstream of the turbine. In black when there is no turbine in the water, and in red when the turbine is underwater and operational. (For interpretation of the references to color in this figure legend, the reader is referred to the Web version of this article.)

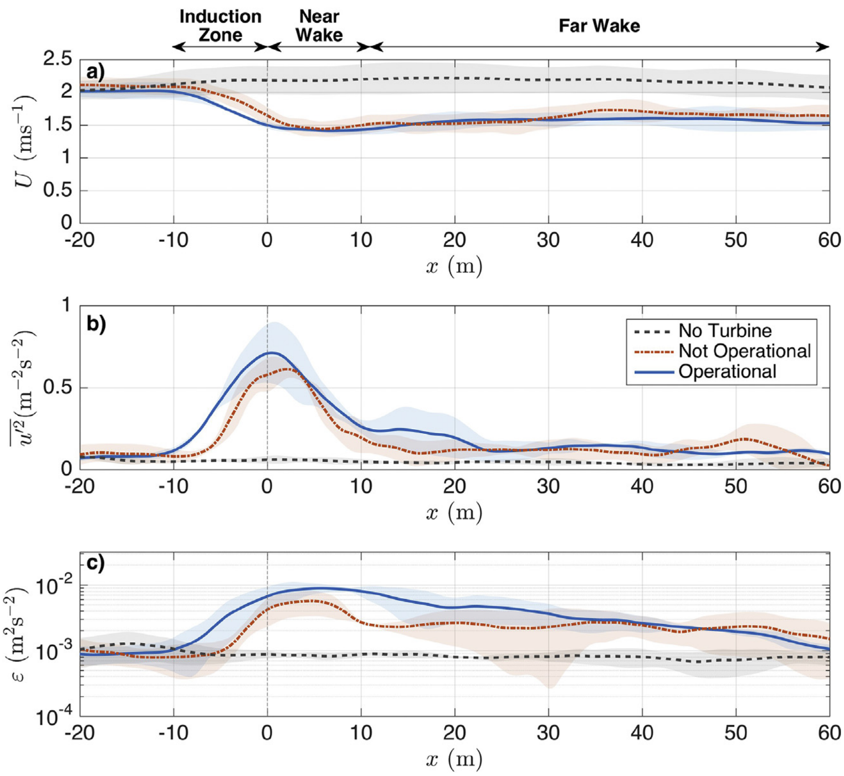

Fig. 15. Hub-height longitudinal profiles of a) Velocity magnitude U, b) Along-channel TKE $\overline{u'^2}$, and c) TKE dissipation rate ε. No turbine in gray, non-operational turbine in red, and operational turbine in blue. Darker lines correspond to a cross-stream average between three streamlines along the turbine wake (turbine port, center, and starboard sides). Shadowed areas represent the standard deviation from the averages along the three streamlines. (For interpretation of the references to color in this figure legend, the reader is referred to the Web version of this article.)

streamlines (a wider shadow indicates a large variation between streamlines).

Prior to turbine deployment, strong lateral shear was observed at hub-height at the turbine location, with stronger flow towards the turbine's starboard side and slower flow towards the turbine's port side. When the turbine is operational the flow decelerates due to turbine blockage and no significant lateral shear is observed just upstream of the turbine location. In the first 10 m of the wake, flow velocity is similar along the three streamlines. After 10 m downstream of the turbine, flow at the center and starboard streamlines increases slightly more than at the port side, which is explained by the faster flows in the starboard side outside of the wake. However, velocities do not recover to their baseline conditions along any of the three streamlines, and any observed increase in velocity is not significant.

Along-channel TKE is observed to have a similar behavior along the three streamlines. Along-channel TKE begins to increase about 10 m upstream of the turbine, and reaches a peak around turbine location. In the first 20 m downstream of the turbine a rapid along-channel TKE decrease is observed. TKE increases again along the starboard streamline around x = 15m, which might be explained by additional TKE shear production in the edges of the wake. TKE fluctuations further downstream are assumed to be caused by natural bathymetric features in the river.

TKE dissipation rates show a behavior consistent with the increase in TKE, peaking about 5 m downstream of the turbine and then slowly decreasing to an undisturbed level about 60 m downstream of the turbine.

From Fig. 15, three regions can be distinguished. From $x = -10$ m to the turbine location at $x = 0$ m, there is an induction zone, where velocity is decreasing while TKE is rapidly increasing. This zone has also been observed upstream of wind turbines, and its extension is related to turbine blockage [39–41]. This region is followed by a near wake up to about $x = 10$ m, where velocity continues to decrease followed by a small amount of recovery, TKE decreases, and TKE dissipation rate peaks. A far wake is observed beyond $x = 10$ m, where both velocity and TKE do not change significantly; the velocity deficit persists, TKE remains slightly elevated with respect to its original level, and TKE dissipation rate continuously decreases. The far wake demonstrates that there is no true recovery of the flow after this turbine, because kinetic energy was extracted from the system. Of course, in some systems potential energy may be converted to kinetic energy, but the total energy is still reduced by extraction.

4.2. Non-operational turbine

The wake observations in Section 3 correspond to the operational turbine conditions. During the life span of any hydrokinetic turbine it is expected that turbines will not be operational for periods of time, due to flow conditions not suitable for energy extraction, to the presence of fauna, or to maintenance, among other reasons. Here, the differences in the wake between operational and non-operational turbine states are examined. Fig. 15 presents longitudinal hub-height profiles for three cases: no turbine, non-operational turbine, and operational turbine. When the turbine is non-operational the induction zone shifts towards the turbine, and velocity reaches its minimum later in the profile, at $x = 8$ m instead of at $x = 2$ m when the turbine is operational. Downstream, no significant differences are observed between these velocity profiles. A similar trend is observed in the TKE profiles; for the non-operational turbine the TKE increases further down in the profile, the TKE maximum is shifted downstream and it is lower than for the operational turbine. These differences are explained by both turbine rotation and turbine energy extraction. Turbine rotation introduces additional turbulence and modifies the flow turbulence length-scales, resulting in higher TKE.

For the non-operational case, the TKE dissipation rate also increases at the turbine location, and remains elevated downstream of the turbine. On average, the dissipation rate remains elevated through the longitudinal extent of the wake, although large cross-wise variations are observed.

The small differences observed in the flow parameters between operational and non-operational cases suggest that the turbine presence as a bluff body in the flow (as opposed to an extractor) is responsible for most of the hydrodynamic impacts in the Kvichak River. The turbine entire structure blocks a high portion of the water column (vertically); this appears to remove a significant portion of power from the flow that is not being converted to useful power, regardless of turbine operation.

4.3. Wake energy loss

The Kvichak River naturally looses energy through the dissipation of turbulent kinetic energy into heat and sound. When the turbine is underwater and operational, it extracts energy from the mean flow and delivers it to the local Igiugig grid. At the same time, more turbulence is generated in the river due to the presence of the turbine and blade rotation. As more turbulence is generated, an increase in TKE dissipation rate is observed in the wake. Thus, the river is loosing additional energy within the turbine wake due to increased TKE dissipation. Here, a volumetric TKE dissipation rate is calculated by multiplying the TKE dissipation rate, ε, by the water density, ρ, and then integrated over the river volume (V) to obtain the rate at which energy is being loss through turbulence as:

$$\text{Rate of Energy Loss} = \int_V \rho\varepsilon \mathrm{d}V \qquad (16)$$

Wake energy loss rates for the three studied cases and their uncertainties are presented in Table 3. Total energy loss rates are calculated in a volume that covers most of the turbine wake: between $x = 0$ m and $x = 60$ m, $y = -14$ m and $y = 14$ m, and from the bottom to the free-surface. Uncertainties are calculated as the sum of each TKE dissipation rate variance (Equation (15)). Energy loss in the turbine region doubles when the turbine is underwater, but non-operational, and triplicates when the turbine is operational. The turbulent energy loss in the wake is comparable to what the rotors extract from the river for electricity generation, which means that the river is loosing as much as twice the energy that is actually being delivered to the community.

4.4. Exergy efficiency

The most used metric for turbine efficiency is the power coefficient, the ratio between the mechanical power extracted by the turbine and the kinetic energy flux through the rotor swept area. From an environmental impacts point of view, a more appropriate performance metric would be the "exergy efficiency" [42]. This efficiency is the ratio between the amount of useful extracted power (turbine extraction) and the change in exergy (useful available power). The large wake energy loss together with the small difference between the operational and non-operational wakes suggest that RivGen is operating at a low exergy efficiency, where most of the power lost by the river is not being transformed into useful power. Considering only the turbine's mechanical power extraction and the amount of energy loss through turbulence in the wake, RivGen's exergy is about 50%.

These results demonstrate that exergy efficiency must be considered in the assessment of large hydrokinetic energy farms, as low exergy efficiency values indicate that a much larger effect on the hydrodynamics of a system exists in addition to what is being extracted by the turbine for electricity production alone.

Table 3
River energy loss rates from turbine extraction and through dissipation of turbulent kinetic energy. Uncertainties are included for the turbulent dissipation values.

Condition	No turbine	Not operational turbine	Operational turbine
Turbulent Dissipation (kW)	3.43 ± 0.04	6.14 ± 0.16	10.93 ± 0.15
Turbine Extraction (kW)	–	–	11.10
Total (kW)	3.43	6.14	22.03

5. Conclusions

Detailed field measurements are used to analyze and understand the evolution of the wake of ORPC RivGen hydrokinetic turbine in the Kvichak River. A drifting Nortek Signature1000 five-beam acoustic Doppler current profiler is used to measure along-beam velocities at high resolution following river streamlines. These observations are used to construct a set of 3D flow conditions in the area surrounding the RivGen turbine for both before turbine deployment and while the turbine is underwater extracting energy.

In general, results show the expected wake characteristics of decreased velocities and increased turbulence downstream of the turbine, however unique wake features are observed. A persistent velocity decrease is observed downstream of the turbine that extends beyond the area covered measurements, demonstrating that there is no wake recovery for this turbine in the Kvichak river. In terms of turbulence parameters, a rapid increase in turbulence intensity, and in turbulent kinetic energy, is observed. The increase in turbulence is consistent with an increase in TKE dissipation rate, which remains elevated through the extent of the wake measurements.

Similar patterns of velocity and turbulence are observed in the wake of a non-operational RivGen turbine, which indicates that the turbine structure removes a significant amount of power even when the turbine is not producing electricity. The TKE dissipation rate parameter allows for the estimation of total energy being loss by turbulence in the wake region. For the operational turbine case, the river looses about the same amount of power via turbulence as via electricity production. These results suggest that the turbine is operating at a low exergy efficiency, where much of power removed from the river is not being delivered to the grid.

This study provides a comprehensive data set of a full-scale cross-flow turbine wake. The methods used in the field are proved to be efficient in characterizing the spatial extent of the wake, at least in system that is in steady state for long periods of time. The observations and analysis presented here serve as validation for numerical models and for future turbine array designs. Most importantly, these results inform turbine designers, project developers, and decision makers about the environmental impacts of hydrokinetic energy extraction under real flow conditions.

All data sets produced for this paper are available in the US Department of Energy Marine and Hydrokinetic Energy data repository website.[2]

[2] https://mhkdr.openei.org/home.

Acknowledgements

The authors thank the support of Joe Talbert, Alex deKlerk, Dylan Dubuque from APL-UW, Sam Harding from PNNL, Eric Nelson from NREL, the people from the village of Igiugig, and the Ocean Renewable Power Company for their help, support and collaboration in this project. This investigation is supported by the U.S. Department of Energy (Award DE-EE0006397) and the Naval Facilities and Engineering Command (Award N00024-10-D-63). Maricarmen Guerra also thanks the support of Fulbright and Becas Chile - Conicyt doctorate fellowship programs.

Appendix A. Steady State Assumption

It is critical for the wake analysis presented here to assume steady state conditions in the Kvichak River. During the measurements period atmospheric conditions were mild and no large rain or flood events were observed. Since there are no stream flow gauges available in the Kvichak River, the steady state assumption is tested using velocity measurements taken upstream of the turbine location through the entire measurement period, and depth variations taken just upstream of the turbine while the turbine was underwater.

True Eulerian velocities taken mid-river between 20 and 30 m upstream of the turbine (within four highly populated grid cells) are used to test the steady state assumption through the measurements period. There were 1054 instantaneous velocity measurements within this location among 9 days of measurements. Turbulent velocities together with daily averages measured at hub-height at this location are shown in Fig. 16. Error bars correspond to one standard deviation from the daily averages. No trend is observed in the daily averaged velocities, and the total averaged velocity from those measurements lies within the error bars through the measurement period.

Data from a HOBO pressure gauges installed on RivGen's frame, just upstream the turbine, are converted to water depth after removing the atmospheric pressure data. Atmospheric pressure measured at the Igiugig Airport weather station (USAF-703061) during the measurements period is shown in Fig. 16a. During the first period of measurements (no turbine in the river), atmospheric pressure remained fairly constant at around 100 kPa. Increased atmospheric pressure, up to 102 kPa, was observed during the non-operational turbine measurements and for the first day of the operational turbine measurements. The effective accuracy from the HOBO pressure gages is 3 cm in depth. The water depth data presented in Fig. 16c show no significant trend. However, high-frequency depth variations between ±5 cm, over a 3.66 m mean depth were observed on July 19–21 2015.

Although there is variability in the flow conditions during the measurements, the steady-state assumption is statistically valid (i.e., none of the variations in the mean values exceed the uncertainties) during the entire measurement period. Furthermore, the upstream variations of order 0.1 ms^{-1} and much smaller than the wake signal, which is order 0.5 ms^{-1}.

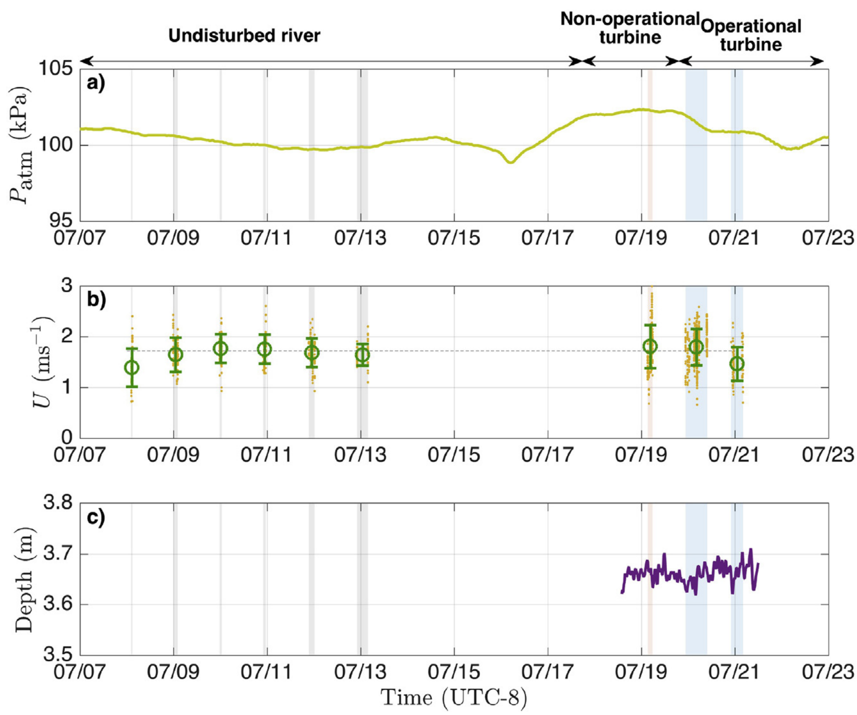

Fig. 16. a) Atmospheric pressure from Igiugig Airport weather station, b) Hub-height velocity upstream of the turbine: instantaneous velocity in orange, daily averages in dark green, and overall average velocity in gray dashed line, and c) water depth measurements upstream of the turbine. In all figures shaded areas correspond with the times of the three data sets from the SWIFT buoy: no turbine (gray), not operational turbine (red), and operational turbine (blue).

References

[1] G. Cada, J. Ahlgrimm, M. Bahleda, T. Bigford, S. Stavrakas, D. Hall, R. Moursund, M. Sale, Potential impacts of hydrokinetic and wave energy conversion technologies on aquatic environments, Fish 32 (2007) 174–181.
[2] G. Boehlert, A. Gill, Environmental and ecological effects of ocean renewable energy development: a current synthesis, Oceanography 23 (2010) 68–81.
[3] B. Polagye, B. Van Cleve, A. Copping, K. Kirkendall, Environmental Effects of Tidal Energy Development: Proceedings of a Scientific Workshop March 22-25, 2010, Technical Report, US National Oceanographic and Atmospheric Administration, 2011.
[4] M. Adaramola, P.-Å. Krogstad, Experimental investigation of wake effects on wind turbine performance, Renew. Energy 36 (2011) 2078–2086.
[5] L. Myers, S. Bahaj, An experimental investigation simulating flow effects in first generation marine current energy converter arrays, Renew. Energy 37 (2012) 28–36.
[6] V.S. Neary, B. Gunawan, C. Hill, L.P. Chamorro, Near and far field flow disturbances induced by model hydrokinetic turbine: ADV and ADP comparison,

Renew. Energy 60 (2013) 1–6.
[7] M. De Dominicis, R.O. Murray, J. Wolf, Multi-scale ocean response to a large tidal stream turbine array, Renew. Energy 114 (2017) 1160–1179.
[8] A.J.G. Brown, S.P. Neill, M.J. Lewis, Tidal energy extraction in three-dimensional ocean models, Renew. Energy 114 (2017) 244–257.
[9] L. Chamorro, C. Hill, S. Morton, C. Ellis, R. Arndt, F. Sotiropoulos, On the interaction between a turbulent open channel flow and an axial-flow turbine, J. Fluid Mech. 716 (2013) 658–670.
[10] S. Kang, X. Yang, F. Sotiropoulos, On the onset of wake meandering for an axial flow turbine in a turbulent open channel flow, J. Fluid Mech. 744 (2014) 376–403.
[11] L. Chamorro, C. Hill, V. Neary, B. Gunawan, R. Arndt, F. Sotiropoulos, Effects of energetic coherent motions on the power and wake of an axial-flow turbine, Phys. Fluids 27 (2015), 055104. 1994-present.
[12] L. Myers, A. Bahaj, Experimental analysis of the flow field around horizontal axis tidal turbines by use of scale mesh disk rotor simulators, Ocean Eng. 37 (2010) 218–227.
[13] W.K. George, The self-preservation of turbulent flows and its relation to initial conditions and coherent structures, Adv. Turbul. 3973 (1989).
[14] P.B. Johansson, W.K. George, M.J. Gourlay, Equilibrium similarity, effects of initial conditions and local Reynolds number on the axisymmetric wake, Phys. Fluids 15 (2003) 603–617.
[15] S. Kang, I. Borazjani, J. Colby, F. Sotiropoulos, Numerical simulation of 3d flow past a real-life marine hydrokinetic turbine, Adv. Water Resour. 39 (2012) 33–43.
[16] T. Blackmore, W. Batten, A. Bahaj, Influence of turbulence on the wake of a marine current turbine simulator, Proc. R. Soc. A 470 (2014), 20140331.
[17] M. Boudreau, G. Dumas, Comparison of the wake recovery of the axial-flow and cross-flow turbine concepts, J. Wind Eng. Ind. Aerod. 165 (2017) 137–152.
[18] S. Chawdhary, C. Hill, X. Yang, M. Guala, D. Corren, J. Colby, F. Sotiropoulos, Wake characteristics of a triframe of axial-flow hydrokinetic turbines, Renew. Energy 109 (2017) 332–345.
[19] L. Myers, A. Bahaj, Wake studies of a 1/30th scale horizontal axis marine current turbine, Ocean Eng. 34 (2007) 758–762.
[20] L. Chamorro, D. Troolin, S. Lee, R. Arndt, F. Sotiropoulos, Three-dimensional flow visualization in the wake of a miniature axial-flow hydrokinetic turbine, Exp. Fluid 54 (2013) 1–12.
[21] P. Bachant, M. Wosnik, Characterising the near-wake of a cross-flow turbine, J. Turbul. 16 (2015) 392–410.
[22] Y. Chen, B. Lin, J. Lin, S. Wang, Experimental study of wake structure behind a horizontal axis tidal stream turbine, Appl. Energy 196 (2017) 82–96.
[23] A. Day, A. Babarit, A. Fontaine, Y.-P. He, M. Kraskowski, M. Murai, I. Penesis, F. Salvatore, H.-K. Shin, Hydrodynamic modelling of marine renewable energy devices: a state of the art review, Ocean Eng. 108 (2015) 46–69.
[24] B. Polagye, R. Cavagnaro, A. Niblick, T. Hall, J. Thomson, A. Aliseda, Cross-flow turbine performance and wake characterization, in: Proc. of the 1st Mar. Energy Technol. Symp. (METS2013), Washington, DC.
[25] M. Rowell, M. Wosnik, J. Barnes, J.P. King, Experimental evaluation of a mixer-ejector marine hydrokinetic turbine at two open-water tidal energy test sites in nh and ma, Mar. Technol. Soc. J. 47 (2013).
[26] B. Gunawan, J. Roberts, V. Neary, Hydrodynamic effects of hydrokinetic turbine deployment in an irrigation canal, in: Proc. of the 3rd Mar. Energy Technol. Symp. (METS2015), Washington, DC.
[27] T. Burton, D. Sharpe, N. Jenkins, E. Bossanyi, Wind Energy Handbook, John Wiley & Sons, 2001.
[28] W. Batten, A. Bahaj, A. Molland, J. Chaplin, The prediction of the hydrodynamic performance of marine current turbines, Renew. Energy 33 (2008) 1085–1096.
[29] D. Forbush, B. Polagye, J. Thomson, L. Kilcher, J. Donegan, J. McEntee, Performance characterization of a cross-flow hydrokinetic turbine in sheared inflow, Int. J. Mar. Energy 16 (2016) 150–161.
[30] D. Forbush, R.J. Cavagnaro, J. Donegan, J. McEntee, B. Polagye, Multi-mode evaluation of power-maximizing cross-flow turbine controllers, Int. J. Mar. Energy 20 (2017) 80–96.
[31] J. Thomson, Wave breaking dissipation observed with SWIFT drifters, J. Atmos. Ocean. Technol. 29 (2012) 1866–1882.
[32] S. Harding, L. Kilcher, J. Thomson, Turbulence measurements from compliant moorings - part I: motion characterization, J. Atmos. Ocean. Technol. 34 (2017) 1235–1247.
[33] L. Kilcher, S. Harding, J. Thomson, S. Nylund, Turbulence measurements from compliant moorings - part II: motion correction, J. Atmos. Ocean. Technol. 34 (2017) 1249–1266.
[34] D. Goring, V. Nikora, Despiking acoustic Doppler velocimeter data, J. Hydraul. Eng. 128 (2002) 117–126.
[35] M. Guerra, J. Thomson, Turbulence measurements from 5-beam acoustic Doppler current profilers, J. Atmos. Ocean. Technol. 34 (2017) 1267–1284.
[36] J. Thomson, B. Polagye, V. Durgesh, M. Richmond, Measurements of turbulence at two tidal energy sites in Puget Sound, WA, IEEE J. Ocean. Eng. 37 (2012) 363–374.
[37] P.J. Wiles, T.P. Rippeth, J.H. Simpson, P.J. Hendricks, A novel technique for measuring the rate of turbulent dissipation in the marine environment, Geophys. Res. Lett. 33 (2006).
[38] P. Rusello, E. Cowen, Turbulent dissipation estimates from pulse coherent Doppler instruments, in: Proc. IEEE/OES 10th Curr., Waves and Turbul. Meas. (CWTM), Monterey, CA., IEEE, pp. 167–172.
[39] D. Medici, S. Ivanell, J.-Å. Dahlberg, P.H. Alfredsson, The upstream flow of a wind turbine: blockage effect, Wind Energy 14 (2011) 691–697.
[40] E. Simley, N. Angelou, T. Mikkelsen, M. Sjöholm, J. Mann, L.Y. Pao, Characterization of wind velocities in the upstream induction zone of a wind turbine using scanning continuous-wave lidars, J. Renew. Sustain. Energy 8 (2016), 013301.
[41] A.R. Meyer Forsting, N. Troldborg, M. Gaunaa, The flow upstream of a row of aligned wind turbine rotors and its effect on power production, Wind Energy 20 (2017) 63–77.
[42] P. Bachant, M. Wosnik, Performance measurements of cylindrical- and spherical-helical cross-flow marine hydrokinetic turbines, with estimates of exergy efficiency, Renew. Energy 74 (2015) 318–325.